A distant real-time radar NDE technique for the in-depth inspection of glass fiber reinforced polymer-retrofitted concrete columns

Tzu-Yang Yu and Oral Buyukozturk

Department of Civil and Environmental Engineering,
Massachusetts Institute of Technology
77 Massachusetts Avenue, Cambridge, MA 02139, U.S.A.

ABSTRACT

A novel real-time radar NDE technique for the in-depth inspection of glass fiber reinforced polymer (GFRP)-retrofitted concrete columns is proposed. In this technique, continuous wave radar signals are transmitted in the far-field region (distant inspection), and reflected signals are collected by the same signal transmitter. Collected radar signals are processed by tomographic reconstruction methods for real-time image reconstruction. In-depth condition in the near-surface region of GFRP-concrete systems is revealed and evaluated by reconstructed images.

Keywords: Radar NDE, distant inspection, GFRP, concrete columns, debonding, tomographic reconstruction

1. INTRODUCTION

Sudden failures of civil infrastructure systems usually lead to significant impacts and catastrophic results in an urban environment. Full knowledge is needed regarding the integrity of a structure at any time in preventing sudden failures of civil structures from happening. Two major approaches are applied; (1) condition assessment of structures, and (2) strengthening and repair of structures. In both approaches, inspection techniques/methodologies are the pivotal capability in the success of these approaches; structural integrity needs to be evaluated in order to perform relevant maintenance, as well as to determine the level of strengthening and repair.

Strengthening and repair of civil infrastructure systems such as concrete structures using fiber reinforced polymer (FRP) has become a major approach in restoring the design capacity and extending the service life of degraded concrete structures for public safety and for effective infrastructure management. Construction defects and structural damages may occur within the FRP-retrofitted concrete structures, especially in the vicinity of FRP-concrete interfaces. Construction defects such as trapped air voids between FRP sheets/plates and concrete substrate are frequently observed during construction. Structural damages such as local debonding of FRP sheets/plates from the concrete surface can also occur under various degrees of confinement pressure and different environmental conditions.[1,2] Both construction defects and structural damages can be considered as near-surface material separation or debonding in the interface vicinity of the FRP-concrete system.

The objective of this paper is to report the development of a far-field airborne radar (FAR) NDT (nondestructive)/NDE technique for the distant inspection of near-surface defects (material separation) in a multi-layered dielectric medium using GFRP-retrofitted concrete columns as an example. This technique utilizes distant (far-field) electromagnetic measurements reflected from the target structure and processes the measurements into reconstructed images for condition assessment. The technique is originally developed for detecting unseen interface defects in GFRP-retrofitted concrete systems, although its capability of detecting reinforcement has also been explored and studied.

In this paper, reported applications of radar (or microwave) NDE in civil engineering are briefly reviewed. Inspection methodology, system design parameters, system components, inspection modes, and data processing

---

Further author information: (Send correspondence to T.-Y. Yu)
E-mail: youngyu@mit.edu, Telephone: 1 617 230 7402

of the FAR NDT technique are provided. Performance of the technique has been validated by laboratory measurements on GFRP-wrapped concrete cylinder specimens with artificial defects and reinforced concrete (RC) cylinder specimens. Features of this technique are summarized in the summary and discussion section.

2. REVIEW OF RADAR NDE APPLICATIONS IN CIVIL ENGINEERING

Radar (radio detection and ranging) NDE is a collective term for NDE techniques using electromagnetic (EM) waves within the radio frequency (RF) spectrum (3Hz~300GHz). Sometimes it is also associated with the microwave NDE techniques using antennas (e.g., horn, parabolic, conical), while the microwave spectrum (300MHz~300GHz) is relatively narrower than the radar spectrum.

In civil engineering, radar signals (EM waves in the RF spectrum) have been used in a variety of applications ranging from material characterization to remote sensing. A survey is performed regarding the current radar NDE applications in civil engineering, as shown in Table 1. From this survey, it is observed that frequencies

Table 1. Survey of radar NDE applications in civil engineering

Application	Frequency	Reference
Material characterization	(0.1~40)MHz (3, 10)GHz (8~12)GHz	3 4 5
Bridge pier scour detection	(0.3, 0.5, 0.9, 1)GHz (0.1~0.5)GHz	6 7
Void and crack detection — Stone and brick masonries — Sluices — Fatigue cracks in steel — Concrete cover — Concrete cracking	 (0.5, 0.9, 1)GHz (0.5, 0.9)GHz (24.125, 33.6)GHz 1.5GHz (3.4~5.8)GHz (2~5.8, 8~12)GHz 1.5GHz 10GHz	 8, 9 10 11 12 13, 14 15 16
Rebar detection	(2~5.8, 8~12)GHz 1GHz	14 17
Structural testing and remote sensing	5.75GHz 10GHz	18 19

used for probing underground and underwater objects are usually less than 1GHz for better penetration but less resolution (effective wavelength in the medium). For detecting anomalies in concrete or masonry structures higher frequencies (greater than 1GHz) are adopted for better resolution but less penetration (skin depth). Frequencies chosen for material characterization are widely distributed due to different targeted characteristic lengths of the material specimen and different experimental configurations.

For the purpose of damage detection in GFRP-concrete systems, a range of frequencies (8GHz~18GHz) has been selected for their wavelengths (3.75cm~1.67cm in free space and 1.53cm~0.68cm in dry concrete using dielectric constant as 6 for concrete) comparable to near-surface defects (e.g., debonding) in the systems; radar signals adjacent to 8GHz aim at the detection of construction defects such as air voids, and the signals adjacent to 18GHz aim at the detection of concrete cracking.

3. FAR-FIELD AIRBORNE RADAR NDE TECHNIQUE

The proposed NDE technique consists of two major components; distant inspection and data processing. Complex responses (amplitude and phase) in the steady state are collected from distant measurements and processed to generate in-depth images for condition assessment. These two components are further explained in the following sections.

3.1 Distant Inspection

In the proposed technique, condition assessment of a target structure is conducted at a range beyond the far-field distance from the structure. The far-field distance, d_{ff}, is generally defined by[20]

$$d_{\text{ff}} = \frac{2D^2}{\lambda} \tag{1}$$

where D is the maximum dimension of radar antenna apertures, and λ is the minimum wavelength of radar signals. Commercial horn antennas have a maximum dimension ranging from 0.2m to 0.4m. Figure 1 shows the calculated d_{ff} of two aperture sizes in the frequency range of 8GHz~12GHz. Radar signals are produced

Figure 1. Far-field distances of two aperture sizes

by a horn antenna and transmitted toward the structure. Reflected radar signals from the structure are then collected by the same antenna (monostatic radar). Figure 2 illustrates the footprint domain G produced by a radar antenna at one position on the synthetic aperture.
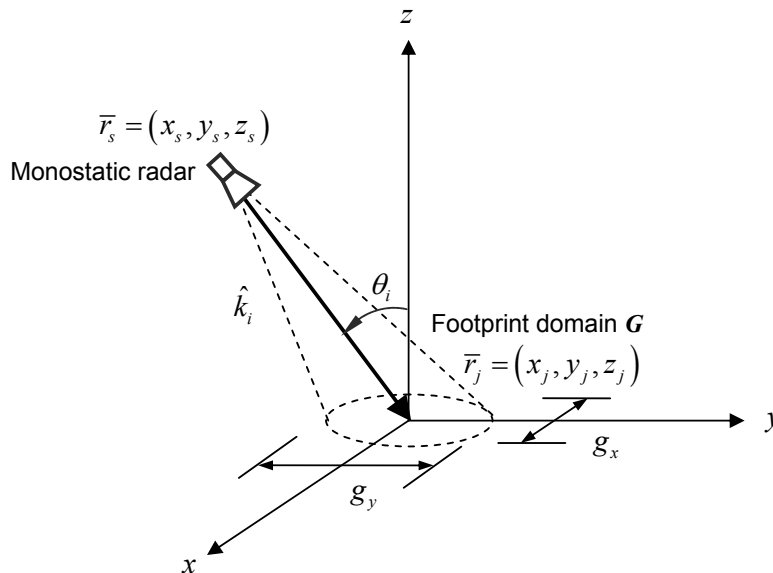

Figure 2. Footprint of ISAR measurements

The footprint domain is characterized by two variables, g_x and g_y, which are related to the radar resolution

in the surface of structures (x-y plane).[21]

$$g_x = \frac{\lambda}{D} R_s \tag{2}$$

$$g_y = \frac{\lambda}{D} \sec \theta_i R_s \tag{3}$$

where $R_s = |\bar{r}_s|$ is the range distance, and θ_i is the inspection/incident angle. Linear and circular flight paths of the radar antenna are termed SAR (synthetic aperture radar) and ISAR (inverse SAR), respectively. Their resolutions in the range (direction of signal propagation) and cross-range (normal to the range direction) directions are summarized in Table 2.[20] λ_c is the wavelength at center frequency, and θ_{int} is the angular range of inspection

Table 2. Range and cross-range resolutions of SAR and ISAR

Radar operation	Range, ρ_r	Cross-range, ρ_{xr}
SAR	$\dfrac{c}{2B}$	$\dfrac{D}{2}$
ISAR	$\dfrac{c}{2B}$	$\dfrac{\lambda_c R_s}{2D} \cong \dfrac{\lambda_c R_s}{2\theta_{\text{int}}}$

angles. These resolutions are used for estimating the needed frequency range (bandwidth) and angular range of the radar measurements. In this technique, ISAR mode of radar operation is adopted, in which the range distance R_s remains unchanged.

3.2 Data Processing – Real-time Image Reconstruction

The data processing method used in the NDE technique is based on ISAR processing[22] and tomographic reconstruction. Backprojection algorithms are used in implementing tomographic reconstruction in the data processing and chosen for their efficiency in image reconstruction.[23]

Once the reflected radar signals are collected for the needed frequency and angular ranges, a data plane (f, θ_i) is constructed, where f denotes measurement frequency. A weighting function is applied to the complex signals in order to reduce the sidelobe levels (evaluated by decibel). The curves of normalized weighting function corresponding to various sidelobe levels (from 30dB to 90dB) are shown in Figure 3. Signals with 200 data points are selected, where the data point 100 corresponds to the center of the antenna. In Figure 3, it is clear that the higher sidelobe reduction the better the signal is focused at the center.

In the ISAR mode, the synthetic aperture is circular (Figure 4(a)), and the radar position vector $\bar{r}_s$ is related to the size of the aperture as shown in Figure 4(b). The scattering response of a point scatterer $\bar{r}_j$ observed by a radar at $\bar{r}_s$ is[21]

$$S(\bar{r}_{s,j}, t) = \frac{1}{R_{s,j}^2} \int_{\omega_c - \pi B}^{\omega_c + \pi B} d\omega \cdot \exp[i\omega t] \tag{4}$$

where $\bar{r}_{s,j} = \bar{r}_s - \bar{r}_j$, $R_{s,j} = |\bar{r}_{s,j}|$, ω_c is the radian center frequency, i is the imaginary number, ω is the radian frequency variable, and t is the time variable. Replacing the time t in $S(\bar{r}_s, t)$ with $\hat{t} = t - \dfrac{2R_s}{c}$ results in the range-compressed $S(\bar{r}_s, \hat{t})$.

In cylindrical coordinate systems where the ISAR motion is convenient to define, the integration of $S(\bar{r}_{s,j}, \hat{t})$ over the structure containing many scatterers provides

$$D(\xi, \hat{t}) = \int_0^{R_s} d\bar{r}_j \int_0^{2\pi} d\phi_i \cdot G(\bar{r}_j, \phi_i) S(\bar{r}_{s,j}, \hat{t}) \tag{5}$$
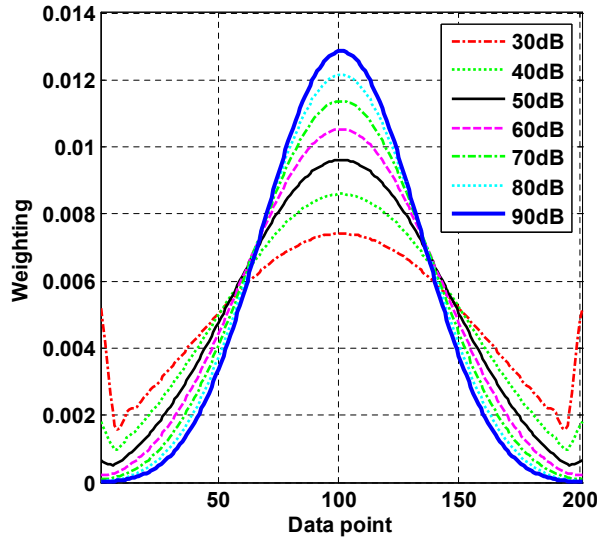
Figure 3. Weighting function curves corresponding to various sidelobe reduction levels

where $\xi = R_s \phi_i$, $G(\bar{r}_j, \phi_i)$ is the scattering amplitude density function at $(\bar{r}_j, \phi_i)$. The backprojection processing is conducted by

$$F(\xi, \hat{t}) = C_{bp} \cdot \frac{\partial D(\xi, \hat{t})}{\partial t} \tag{6}$$

where C_{bp} is the backprojection coefficient to yield an ideal bandpass transfer function. A matched filter $M(\hat{t} - t')$ is first applied on $D(\xi, \hat{t})$ to improve the processing efficiency and to avoid discontinuity in $D(\xi, \hat{t})$ such that

$$\frac{\partial D(\xi, \hat{t})}{\partial t} = \frac{\partial}{\partial t} \int\limits_0^{\hat{t}} dt' \cdot D(\xi, \hat{t}) \cdot M(\hat{t} - t') = \int\limits_0^{\hat{t}} dt' \cdot D(\xi, \hat{t}) \cdot \frac{\partial M(\hat{t} - t')}{\partial t} \tag{7}$$

where $\dfrac{\partial M(\hat{t} - t')}{\partial t}$ can be computed before the measurements are collected and processed to obtain $D(\xi, \hat{t})$. Such computational advantage lays the foundation for real-time processing. Finally, the reconstructed image is obtained by

$$I(\bar{r}, \phi) = \int\limits_0^{R_s \theta_{\text{int}}} d\xi \cdot F(\xi, \hat{t}) \tag{8}$$

where $(\bar{r}, \phi)$ is defined on the range vs. cross-range images of the structure. The spatial information derived from $\hat{t}$ can be obtained by $\bar{r} = c\hat{t}$ for a given inspection angle θ_i. The time-shifting processing is equivalent to the space-projection processing in this context. The range direction is in parallel with the depth of the structure and the cross-range direction is normal to the depth, the range vs. cross-range images provide the in-depth information of the structure.

Computational cost of this data processing algorithm is considered minimum. For example, the needed time for processing a 201×301 size data set on a machine with a 1.6GHz CPU and 512MB of RAM in the Matlab environment on the Windows XP platform is about 2.6 sec. The computational cost can be further reduced with better hardware capability.

4. VALIDATION BY LABORATORY MEASUREMENTS

The feasibility and performance of the NDE technique is validated and examined using laboratory measurements on GFRP-retrofitted concrete cylinder specimens. Four cylinder specimens (two GFRP-concrete cylinders with

(a) Inverse synthetic aperture radar (ISAR)
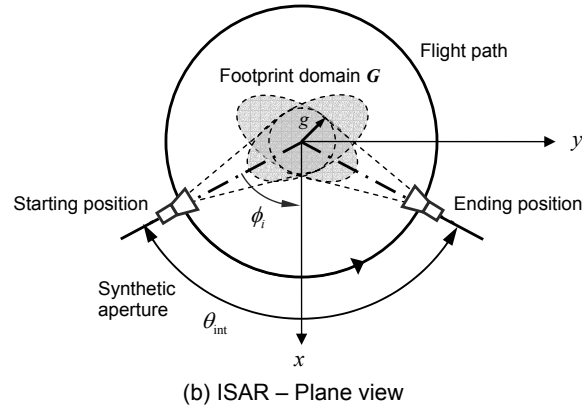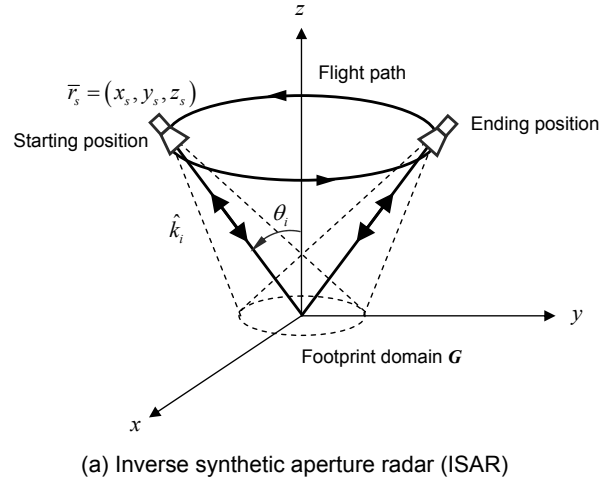

(b) ISAR – Plane view

Figure 4. Inverse synthetic aperture radar

artificial defects, one reinforced concrete cylinder, and one plain concrete cylinder) were manufactured and subjected to laboratory far-field ISAR measurements. Details of laboratory measurements are provided in the following sections.

4.1 Specimen Preparation

Four specimens were designed and manufactured for laboratory far-field ISAR measurements; specimen AD1: GFRP-wrapped concrete cylinder with artificial defect type 1, specimen AD2: GFRP-wrapped concrete cylinder with artificial defect type 2, specimen RE: concrete cylinder with four rebars, and specimen PC: plain concrete cylinder. Portland Type I cement was used, and the mix ratio of concrete was water:cement:sand:aggregate = 0.45:1:2.52:3.21 (by weight). The diameter of concrete core was 15.24 cm, and the heights were 30.4 cm and 38.1 cm. Specimens AD1 and AD2 are shown in Figure 5, and specimens RE and PC are shown in Figure 6. Concrete cores of these specimens were cast with different configuration scenarios (e.g., artificial defect, rebar) and cured in clean water for 14 days. Artificial defect type 1 was a cubic-like Styrofoam (3.81cm-by-3.81cm-by-2.54cm), and artificial defect type 2 was a delamination-like Styrofoam (7.62cm-by-7.62cm-by-0.51cm). These two artificial defects were placed in the interface between GFRP sheet and concrete substrate in the GFRP-concrete specimen. After the curing period the concrete cores were wrapped with GFRP sheet according to the manufacturer's specifications. A unidirectional glass fabric system (TyfoR SEH-51A by Fyfe Co. LLC) was used and molded with epoxy resin (TyfoR S Epoxy) to form the GFRP-epoxy sheet wrapped on the surface of the concrete core. The volumetric ratio of epoxy:GFRP was 0.645:0.355. The thickness of the GFRP-epoxy sheet was 0.25 cm. Single layer configuration scheme was adopted. Specimen RE was manufactured with four No.3

steel rebars (diameter = 0.95 cm) positioned at four angles with different cover depths (0 : 0.25 cm / 90 : 1.27 cm / 180 : 2.54 cm / 270 : 3.81 cm).
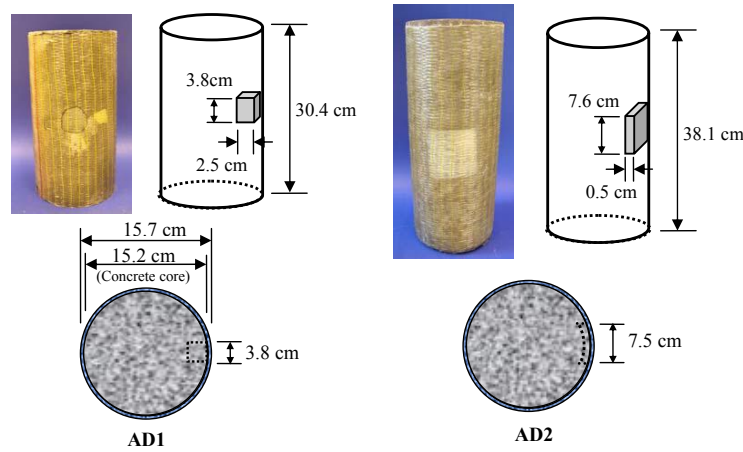

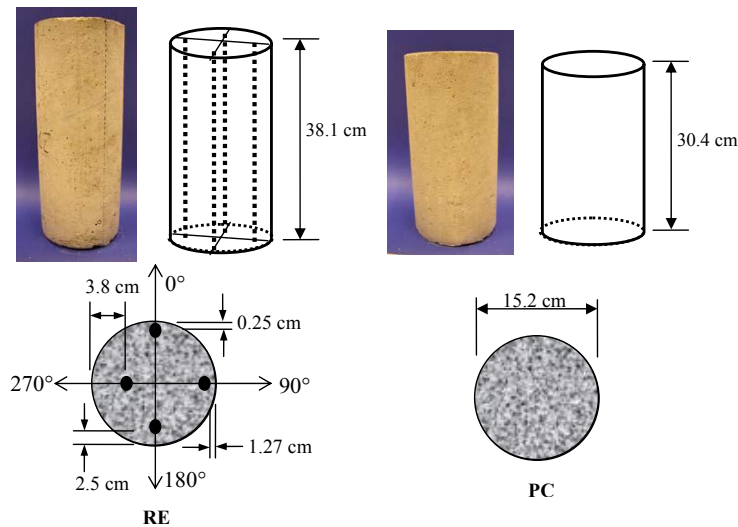Figure 5. Laboratory concrete specimens AD1 and AD2

Figure 6. Laboratory concrete specimens RE and PC

4.2 Experimental Configuration

Radar measurements of the GFRP-confined concrete specimens were performed at the MIT (Massachusetts Institute of Technology) Lincoln Laboratory using the Compact RCS/Antenna Range facility. The experimental set-up mainly consists of a horn antenna, stepped-frequency radar, network analyzer systems, and a Harris dual-shaped reflection system, Model 1606, designed for conducting far-field measurements. The purpose of this reflection system is to produce plane waves in the limited space of laboratory. A schematic description of laboratory configuration is provided in Figure 7. The reflection system would not be required for field measurements. This facility can achieve high signal-to-noise ratio for a large frequency bandwidth ranging from UHF (0.7GHz) to 100GHz. The radar system is capable of producing a 20-m quiet zone, different antenna radiation patterns, and full polarimetric RCS (radar cross section) measurements. Calibration of the far-field measurement is carried out with respect to the surface of the target structure. Signal-to-noise ratio (SNR) is enhanced by the coherent, wide bandwidth measurements in this technique. Radar measurements were conducted at X-band (8GHz ~ 12GHz) frequencies to achieve optimized resolution and surface penetration capabilities.
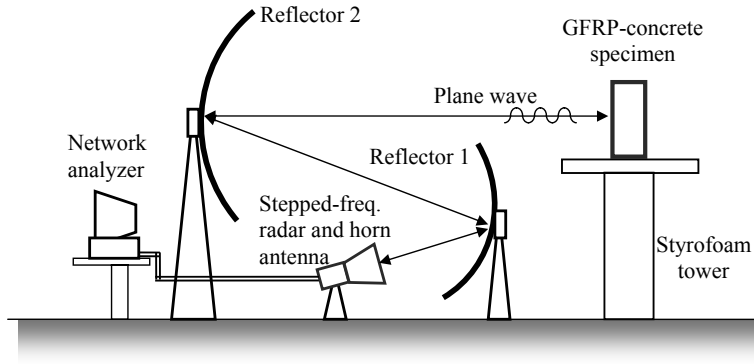
Figure 7. Schematic illustration of the laboratory far-field ISAR measurements

The range resolution is directly related to the bandwidth of radar signals. Two types of linear polarizations are used in the radar measurements: HH (transverse electric or TE) and VV (transverse magnetic or TM). Sinusoidal signals were used, and steady-state complex responses (amplitude and phase) were collected. Each complex response data point took 0.7 sec (per frequency per angle) to record in the laboratory configuration.

The measurements were conducted in stepped-frequency mode by sweeping from a starting frequency to an end frequency in an increment of 0.02GHz at a fixed angle. The specimen was then rotated to the next angular step, and the frequency sweeping was again performed (Fig. 3). The total rotation (range of azimuth angle), θ_{int}, in the ISAR measurements was 30° and 60°, and angular increments was 0.2°. Frequency-angle data showing the reflection response in decibel (dB) were recorded.

Two measurement schemes were investigated; normal incident (Figure 8) and oblique incident (Figure 9). The relative movement of a rotating Styrofoam tower with respect to a fixed radar simulated the relative motion of a moving radar with respect to a fixed structure. Specimens AD1 and AD2 were measured in the oblique incident scheme for debonding detection, and specimens RE and PC were measured in the normal incident scheme for rebar detection.
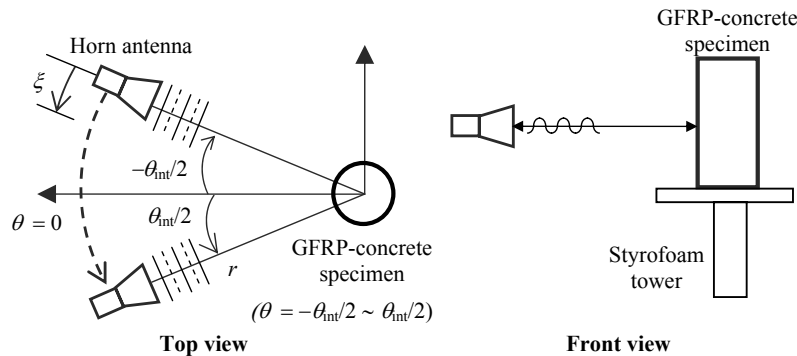

Figure 8. Normal incident scheme of the laboratory far-field ISAR measurements

4.3 Reconstructed Images

4.3.1 Debonding Detection

For detecting debonding defects the reconstructed images using far-field ISAR measurements of specimens AD1 and AD2 are considered. Although both HH and VV polarizations of radar signals are used, only HH polarization results are reported in this paper.

Three reconstructed images are shown in Figure 10, using the far-field ISAR measurements which are illustrated in Figure 11. In these images, location of the specimen is highlighted with a solid line rectangle. These
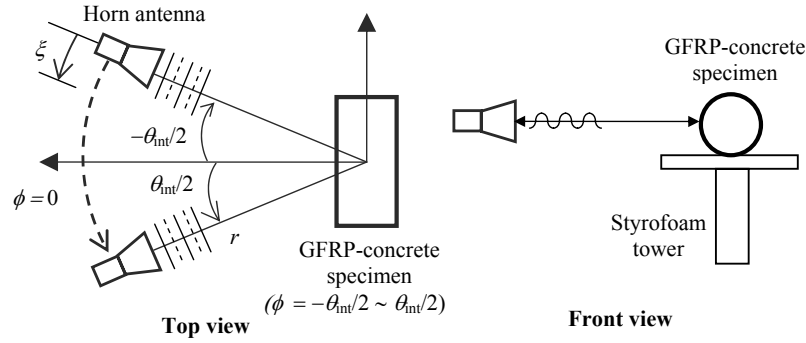
Figure 9. Oblique incident scheme of the laboratory far-field ISAR measurements

images are generated using the measurements at the inspection angle = 10°. Figure 10(a) is the image reconstructed by the measurements of the intact side of specimen AD1. It is used as an reference image to represent the intact part of a structure. The reason is that, in a practical inspection scenario, comparison between two identical civil structures (one intact and the other damaged) can be rarely conducted. Rather, comparison can be performed either between two locations (one intact and the other damaged) of a structure or between the measurements of one location of a structure at two different time instants. The later case leads to the application of structural health monitoring. In Figure 10(a) two red scattering signals are revealed as the result of
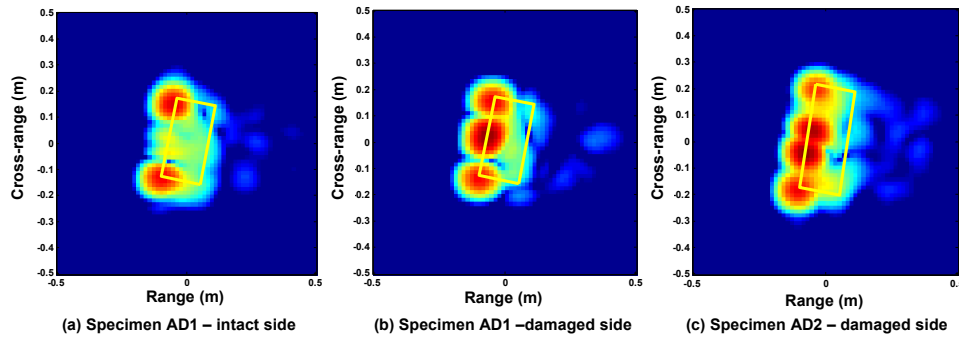

(a) Specimen AD1 – intact side (b) Specimen AD1 –damaged side (c) Specimen AD2 – damaged side

Figure 10. Reconstructed images of specimens AD1 and AD2

(a) Specimen AD1 – Intact side (b) Specimen AD1 – Damaged side (c) Specimen AD2 – Damaged side
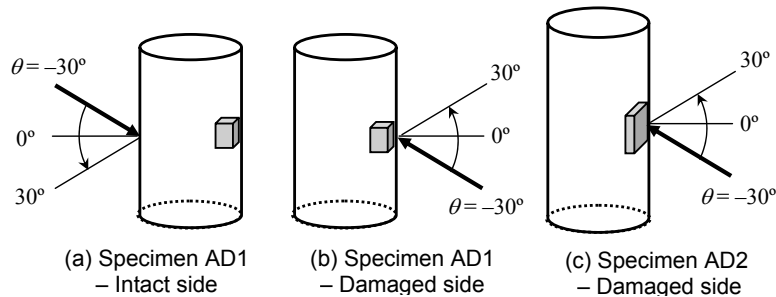
Figure 11. Description of the far-field ISAR measurements of specimens AD1 and AD2

edge reflection from the finite specimen. In practice, the size of civil structures will eliminate these background scattering signals from the image. With this knowledge, the middle scattering signal in Figure 10(b) indicates the presence of the cubic-like anomaly, whose center coincides with the actual location of the embedded anomaly.

Figure 10(c) shows the detailed features of the anomaly as the observed two scattering signals (two edges of the anomaly) in the image. This demonstrates the detection capability of the proposed distant NDE technique.

4.3.2 Rebar Detection

The capability of detecting steel rebars by the technique is demonstrated comparing two reconstructed images of specimens PC (without rebars) and RE (with four rebars). Normal incident scheme was chosen in order distinguish the location of the rebars on the plane perpendicular to their orientation. HH-polarized X-band measurements were used for image reconstruction. The reconstructed images of the specimens are shown in Figure 12 with a solid line circle indicating the location of the specimen. It is observed, in Figure 12(a),
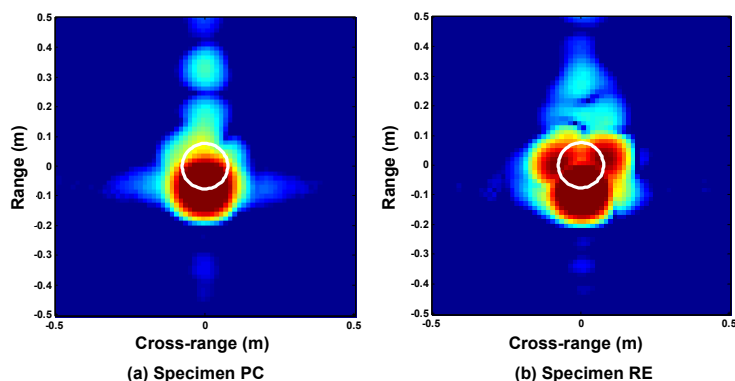

(a) Specimen PC   (b) Specimen RE

Figure 12. Reconstructed images of specimens RE and PC

the specular effect/return produces a strong scattering signal at the edge of the specimen closet to the radar. Although the presence of the rebars is also revealed by scattering signals as shown in Figure 12(b), the scattering signal within the range of specular effect is unlikely to be discovered. However, on the other hand, the presence of adjacent rebars is clearly indicated by two scattering signals. The rebar in the back (with respect to the radar) has a concrete depth of about 14 cm (5.5 in), whose scattering signal is too weak to be detected.

5. SUMMARY AND DISCUSSION

The proposed distant radar NDE technique for condition assessment of GFRP-retrofitted concrete structures consists of two components: (1) far-field ISAR measurements in two schemes and (2) data processing algorithm. In this paper, work is reported on laboratory radar measurements of GFRP-concrete specimens in the far-field region at different angles in the frequency range 8GHz∼12GHz. The measured frequency-angle data are processed by the imaging algorithm (backprojection algorithm) to reconstruct the range-cross-range imagery of the structure, which serves as a basis for condition assessments to detect near-surface defects and debonding, as well as rebars in the specimen. Research findings are summarized as follows.

- **Validity of the technique** – This work validates the feasibility of a distant radar NDE technique for the in-depth inspection of GFRP-concrete structures. It is shown that, with optimized bandwidth and angular ranges, near-surface defects including air voids and delaminations as well as existing rebars can be detected.

- **Distant inspection** – The far-field distance (Figure 1) in the frequency range of 8GHz∼12GHz ranges from 2 m to 3.25 m for an aperture size of 0.2 m. For most in-field inspection, 4 m of separation distance can be easily achieved. This suggests the use of relevant aperture size of the radar to satisfy the far-field distance requirement. However, it is the distant inspection feature offered by this technique applicable for the structures whose accessibility may be difficult and expensive, such as cross-river concrete bridge piers.

- **Real-time processing** – The computational cost on a machine with a 1.6GHz CPU and 512MB of RAM in the Matlab environment on the Windows XP platform is about 2.6 sec. The computational cost can be further reduced with better hardware capability. This feature allows the inspector to almost-immediately evaluate the performance of assessment on the site. The need for additional measurements can be quickly decided, and the results can also be evaluated.

6. ACKNOWLEDGMENTS

REFERENCES

[1] Au, C. and Buyukozturk, O., "Peel and shear fracture characterization of debonding in frp plated concrete affected by moisture," *ASCE J. Compos. Constr.* **10**(1), 35–47 (2006).

[2] Buyukozturk, O. and Yu, T.-Y., "Understanding and assessment of debonding failures in frp-concrete systems," in *Proc. of Seventh Intl. Congress on Advances in Civil Eng.*, Yildiz Tech. Univ. Press, Istanbul, Turkey (2006).

[3] Al-Qadi, I. L., Hazim, O. A., and Riad, S. M., "Dielectric properties of portland cement concrete at low radio frequencies," *ASCE J. Mater. Civil Eng.* **7**(3), 192–8 (1995).

[4] Bois, K. J., Benally, A. D., and Zoughi, R., "Microwave near-field reflection properties analysis of concrete for material content determination," *IEEE Trans. Instrum. Meas.* **49**(1), 49–55 (2000).

[5] Arunachlam, K., Melapudi, V. R., Upda, L., and Upda, S. S., "Microwave ndt of cement-based materials using far-field reflection coefficients," *NDT&E Intl.* **39**(7), 585–93 (2006).

[6] Millard, S. G., Bungey, J. H., Thomas, C., Soutos, M. N., Shaw, M. R., and Patterson, A., "Assessing bridge pier scour by radar," *NDT&E Intl.* **31**(4), 251–8 (1998).

[7] Forde, M. C., McCann, D. M., Clark, M. R., Broughton, K. J., Fenning, P. J., and Brown, A., "Radar measurement of bridge scour," *NDT&E Intl.* **32**(8), 481–92 (1999).

[8] Binda, L., Lenzi, G., and Saisi, A., "Nde of masonry structures: use of radar tests for the characterization of stone masonries," *NDT&E Intl.* **31**(6), 411–9 (1998).

[9] Maierhofer, C. and Leipold, S., "Radar investigation of masonry structures," *NDT&E Intl.* **34**(2), 139–47 (2001).

[10] Maierhofer, C., Krause, M., and Wiggenhauser, H., "Non-destructive investigation of slucies using radar and ultrasonic impulse echo," *NDT&E Intl.* **31**(6), 421–7 (1998).

[11] Qaddoumi, N., Ranu, E., McColskey, J. D., Mirshahi, R., and Zoughi, R., "Microwave detection of stress-induced fatigue cracks in steel and potential for crack opening determination," *Res. Nondestr. Eval.* **12**, 83–103 (2000).

[12] Klysz, G., Balayssac, J.-P., and Laurens, S., "Spectral analysis of radar surface waves for non-destructive evaluation of cover concrete," *NDT&E Intl.* **37**(3), 221–7 (2004).

[13] Buyukozturk, O. and Rhim, H. C., "Radar measurements of concrete for nondestructive evaluation of dams," in *Proc. of SPIE*, **2457**, 168–74, SPIE (1995).

[14] Rhim, H. C. and Buyukozturk, O., "Wideband microwave imaging of concrete for nondestructive testing," *ASCE J. Struct. Eng.* **126**(12), 1451–7 (2000).

[15] Maierhofer, C., Brink, A., Rollig, M., and Wiggenhauser, H., "Detection of shallow voids in concrete structrues with impulse thermography and radar," *NDT&E Intl.* **36**(4), 257–63 (2003).

[16] Nadakuduti, J., Chen, G., and Zoughi, R., "Semiempirical electromagnetic modeling of crack detection and sizing in cement-based materials using near-field microwave methods," *IEEE Trans. Instrum. Meas.* **55**(2), 588–97 (2006).

[17] Shaw, M. R., Millard, S. G., Molyneaux, T. C. K., Taylor, M. J., and Bungey, J. H., "Location of steel reinforcement in concrete using ground penetrating radar and neutral networks," *NDT&E Intl.* **38**(3), 203–12 (2005).

[18] Pieraccini, M., Luzi, G., Mecatti, D., Fratini, M., Noferini, L., and Carssimi, L., "Remote sensing of building structural displacements using a microwave interferometer with image capability," *NDT&E Intl.* **37**(9), 545–50 (2004).

[19] Shinozuka, M., Ghanem, R., Houshmand, B., and Mansouri, B., "Damage detection in urban areas by sar imagery," *ASCE J. Eng. Mech.* **126**(7), 769–77 (2000).

[20] Knott, E. F., Shaeffer, J. F., and Tuley, M. T., *Radar Cross Section*, SciTech Publishing, Rayleigh, NC (2004).

[21] Tsang, L., Kong, J. A., and Ding, K.-H., *Scattering of Electromagnetic Waves – Theories and Applications*, John Wiley & Sons, New York (2000).

[22] Soumekh, M., *Synthetic Aperture Radar Signal Processing with MATLAB algorithms*, Wiley, New York, NY (1999).

[23] Yegulalp, A. F., "Fast backprojection algorithm for synthetic aperture radar," in *Proc. of IEEE Radar Conf.*, 60–5, IEEE (1999).